ACS APPLIED MATERIALS & INTERFACES

Research Article

www.acsami.org

Highly Transparent and Flexible Triboelectric Nanogenerators with Subwavelength-Architectured Polydimethylsiloxane by a Nanoporous Anodic Aluminum Oxide Template

Bhaskar Dudem, Yeong Hwan Ko, Jung Woo Leem, Soo Hyun Lee, and Jae Su Yu*

Department of Electronics and Radio Engineering, Kyung Hee University, 1732 Deogyeong-daero, Giheung-gu, Yongin-si 446-701, South Korea

Supporting Information

ABSTRACT: Highly transparent and flexible triboelectric nanogenerators (TENGs) were fabricated using the subwavelength-architectured (SWA) polydimethylsiloxane (PDMS) with a nanoporous anodic aluminum oxide (AAO) template as a replica mold. The SWA PDMS could be utilized as a multifunctional film for a triboelectric layer, an antireflection coating, and a self-cleaning surface. The nanopore arrays of AAO were formed by a simple, fast, and cost-effective electrochemical oxidation process of aluminum, which is relatively impressive for fabrication of the TENG device. For electrical contacts, the SWA PDMS was laminated on the indium tin oxide (ITO)-coated polyethylene terephthalate (PET) as a bottom electrode, and the bare ITO-coated PET (i.e., ITO/PET) was used for the top electrode. Compared to the ITO/PET, the SWA PDMS on the ITO/PET improved the transmittance from 80.5 to 83% in the visible wavelength region and also had high transmittances of >85% at wavelengths of 430−455 nm. The SWA PDMS also exhibited the hydrophobic surface with a water contact angle (θ_{CA}) of ∼115°, which can be useful for self-cleaning applications. The average transmittance (T_{avg}) of the entire TENG device was observed to be ∼70% over a broad wavelength range. At an external pushing frequency of 0.5 Hz, for the TENG device with the ITO top electrode, open-circuit voltage (V_{OC}) and short-circuit current (I_{SC}) values of ∼3.8 V and ∼0.8 μA were obtained instantaneously, respectively, which were higher than those (i.e., $V_{OC} \approx 2.2$ V, and $I_{SC} \approx 0.4$ μA) of the TENG device with a gold top electrode. The effect of external pushing force and frequency on the output device performance of the TENGs was investigated, including the device robustness. A theoretical optical analysis of SWA PDMS was also performed.

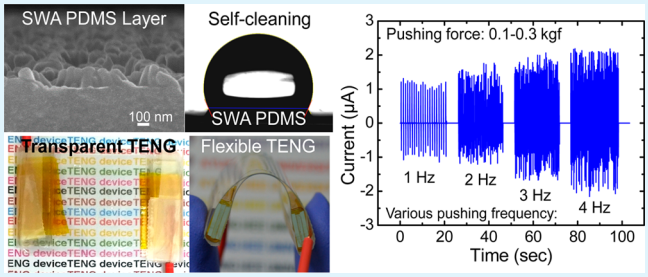

KEYWORDS: *transparency, triboelectric nanogenerators, subwavelength architectured PDMS, anodic aluminum oxide*

INTRODUCTION

Energy conversion technology from ambient environment sources into electrical energy is one of great interest in various renewable energy applications, and it has been expected to be the foremost substitution for conventional power supplies.[1−3] Currently, nanogenerators have exhibited a promising potential to efficiently convert different forms of energy into electricity using piezoelectric, trioelectric, electromagnetic, and pyroelectric effects.[4−7] In particular, most of the researchers in this field have growing interest in triboelectric nanogenerators (TENGs) because of their conversion efficiency of various mechanical energies observed in our daily lives such as human motion,[8,9] mechanical triggering,[10−12] rotation,[13,14] etc. According to the general operation principle of TENGs, electron flow can take place by the triboelectric effect-induced electrostatic charges on the surfaces of two different triboelectric materials.[15] However, there are still technological demands for the next generation of flexible and transparent device applications. Triboelectric nanogenerators can be also utilized for various applications such as self-powered sensors to recognize human motion/pressure, voice recognition, transportation monitoring, etc.[16−21] Many research groups demonstrated flexible and transparent piezoelectric zinc oxide (ZnO)-based nanogenerators, but the design of devices is somewhat complex in connection with sophisticated operations.[22,23]

Recently, flexible TENGs based on polymer materials have been developed rapidly because of their simple and cost-effective design process with high-output performance as compared to that of other nanogenerators as power sources.[24−28] These flexible TENGs have been demonstrated by employing micro- and nanopatterned polymer materials such as polydimethylsiloxane (PDMS) as a triboelectric material, where the indium tin oxide (ITO)-coated polyethylene terephthalate (PET) or gold (Au) is used as an electrode. In general, the patterned PDMS surface plays a key role in increasing the separation efficiency and the friction area between the polymer materials and electrodes, thereby improving the device efficiency.[27,29,30] Simultaneously, these

Received: January 30, 2015
Accepted: August 24, 2015
Published: August 24, 2015

DOI: 10.1021/acsami.5b05842
ACS Appl. Mater. Interfaces 2015, 7, 20520−20529

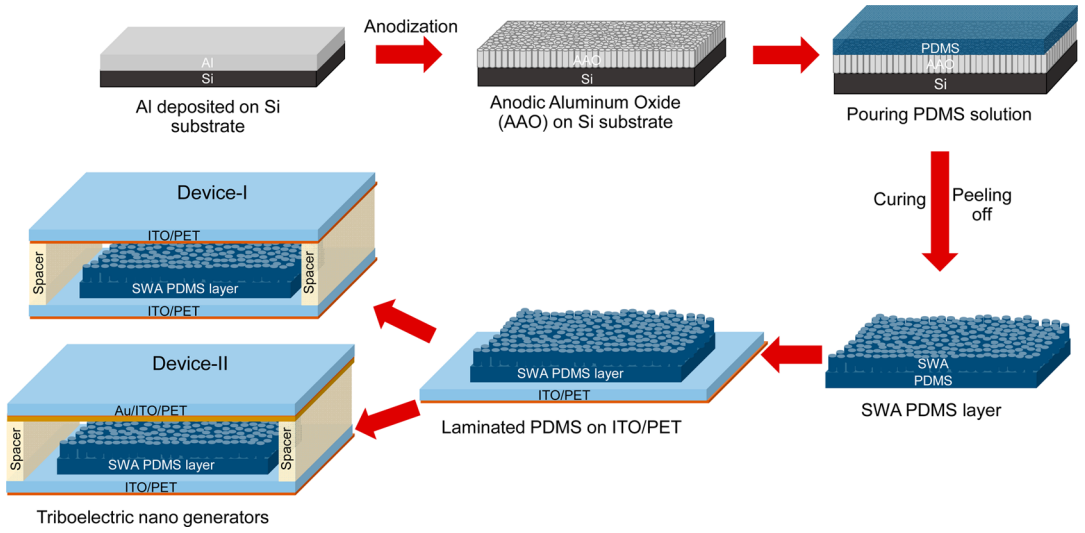

Figure 1. Schematic for the fabrication of the TENG device with the SWA PDMS layer laminated on the ITO/PET substrate as a bottom electrode and the bare ITO/PET as a top electrode. The schematics of two different TENG devices (Device-I and Device-II) are also shown.

patterned structures on the PDMS can also improve the transparency of the TENGs with a transparent conductive oxide-coated film like the ITO because of the antireflection property of patterned PDMS.[27] To prepare the micro- or nanopatterns on the surface of PDMS using soft lithography, silicon (Si) or sapphire molds have been generally employed. However, the fabrication of these patterned surfaces involves expensive processing techniques such as photolithography,[29] electron-beam lithography,[31] nanoimprinting lithography,[32] laser interference lithography,[33,34] etc., including a subsequent dry etching. Moreover, the fabrication process of these molds is complicated and time-consuming. On the other hand, a nanoporous anodic aluminum oxide (AAO) template is one of the best alternatives to these molds. The AAO templates have been prepared by a simple, fast, and cost-effective electrochemical oxidation process (anodization) of aluminum (Al) under certain electrolyte conditions. The AAO is an aluminum oxide (Al_2O_3) film with self-organized and closely packed cylindrical nanopores.[35,36]

In this work, we reported the triboelectric characteristics of a highly transparent and flexible PDMS layer with subwavelength architectures (i.e., SWA PDMS) fabricated by a soft lithography technique via the porous AAO template as a mold. The SWA PDMS improves the transparent property of TENG devices in the broad visible and near-infrared wavelength range of 400–1000 nm as well as the efficient friction surface compared to the bare flat PDMS. Besides, it can be easily prepared by the mass-production soft lithography method that combines low cost and short time with large scalability because once AAO molds are fabricated, they can be repeatedly used for pattern formations on the PDMS surface. In addition, because of the detachability of the PDMS on any flat transparent substrates, the damaged SWA PDMS can be just replaced into a new one in TENG device systems. Also, the SWA PDMS with a hydrophobic surface can be utilized in self-cleaning applications. In this point, we proposed the highly roughened SWA PDMS that offers an efficient surface for triboelectric charge generation as well as a high transparency. Optical properties of the SWA PDMS layer on ITO/PET were measured and also studied therotically using a rigorous coupled-wave analysis (RCWA) simulation. The SWA PDMS layer was laminated on the ITO/PET to fabticate highly transparent and flexible TENG devices, and their output voltage and current performances were explored.

EXPERIMENTAL DETAILS

Figure 1 shows the schematic for the fabrication of the TENG device with the SWA PDMS layer laminated on the ITO/PET substrate as a bottom electrode and the bare ITO/PET as a top electrode. To prepare the SWA PDMS, the nanoporous AAO template on Si (i.e., AAO/Si) as a replica mold was used. The AAO template was fabricated by the anodization of an Al thin film with a thickness of 200 nm that was deposited on the Si substrate by using an electron-beam evaporation system at room temperature. The Al thin film was further anodized using a 5 wt % H_3PO_4 electrolyte solution at an applied dc voltage of 75 V, and the pore widening treatment was conducted by dipping the anodized samples for 10 min into a 5 wt % phosphoric acid solution at 30 °C, which forms AAO nanopore arrays. During the anodization process, the temperature of the electrolyte was maintained at 2 °C. Then, the surface of the anodized sample (i.e., AAO template) was treated with trimethylchlorosilane gas phase silanization for 4 h to prevent the PDMS film from sticking to the porous AAO. Furthermore, the random nanopatterns on the template were transferred by spin-coating the hard PDMS (*h*-PDMS, prepared by mixing VDT-731, SIP 6831.1, SIT 7900, and HMS-301 from Gelest, Inc.) on the surface of AAO/Si substrate and then cured in an oven at 75 °C for 20 min. Subsequently, the soft PDMS (*s*-PDMS, a mixture of base resin and curing agent of Sylgard 184 silicone elastomer) was also spin-coated on the *h*-PDMS/AAO/Si substrate and cured again at 80 °C for 2 h. Here, we spin-coated two different PDMS (*h*- and *s*-PDMS) layers on the AAO/Si mold under different spin-coating conditions (as mentioned in the Supporting Information). As compared to the *s*-PDMS with a low modulus of ~2 N/mm^2, the *h*-PDMS with a high modulus (~9 N/mm^2) and a low surface energy could be useful for replicating high-density nanoporous structures on the AAO at a 100 nm scale without any distortion and deformation,[37,38] but it is difficult to handle a thin (~30 μm) and stiff layer of *h*-PDMS.[39] Therefore, the *s*-PDMS was spin-coated on the stiff *h*-PDMS as a protecting layer and allows for manual application, in a nondestructive manner.[40,41] Finally, a thermally cured PDMS (*h*-/*s*-PDMS) layer containing the SWAs on the surface was peeled off from the AAO/Si substrate. Subsequently, the SWA PDMS layer was carefully laminated on the insulation surface of a clean ITO-coated PET substrate, and then the entire structure was covered with another ITO-coated PET film (or Au-coated ITO/PET film) to form the sandwich-structured TENG devices, as shown in Figure 1. It is noted

DOI: 10.1021/acsami.5b05842
ACS Appl. Mater. Interfaces 2015, 7, 20520–20529

that the SWA PDMS surface and the ITO electrode (or Au electrode) are placed face to face and separated by leaving a 3 mm gap between two contact surfaces using glass spacers. The device fabrication process is very simple and low-cost, and it can be useful for large-scale production industries. For comparison, the bare PDMS with the flat surface was also prepared by the same process, and then it was also applied to TENG devices.

The structural and morphological properties of the AAO template fabricated on Si substrates and the SWA PDMS replicated by AAO templates were observed by using a field-emission scanning electron microscope (FE-SEM) (LEO SUPRA 55, Carl Zeiss) measurements. The transmittance nature of the samples was evaluated by using a UV−vis−NIR spectrophotometer (Cary 5000, Varian) with an integrating sphere at normal incidence. The water contact angles were measured and averaged at three different positions on the surface of samples by using a contact angle measurement system (Phoenix-300, SEO Co., Ltd.) with ∼5 μL droplets of deionized water at room temperature. For theoretical analysis of the SWA PDMS on the ITO/PET substrate, optical modeling and simulation were performed by the RCWA method using a commercial software (*DiffractMOD*, Rsoft Design Group). To design the theoretical models, the PDMS layer with subwavelength architectures was approximately considered as cylindrical pattern arrays with a periodic 4-fold rectangular symmetry, for the sake of simplicity. The generated open-circuit voltage (V_{OC}) and short-circuit current (I_{SC}) of the fabricated TENG device were measured by using a programmable Keithley 2000 system as a multimeter and a Keithley 6487 system as a picoammeter, respectively. An indicator with a load cell (BONGSHIN, Inc.) was used to monitor the external pushing force applied on the top electrode of TENG devices.

RESULTS AND DISCUSSION

To investigate the influence of SWA PDMS laminated on ITO/PET on the total transmittance, the RCWA simulation was performed. Figure 2a shows the contour plot of the calculated transmittance spectra by considering a simple three-dimensional (3D) scale-modified simulation model with periodic 4-fold rectangular symmetry SWA arrays (also shown in Figure 2a). We assumed that the each thickness of PDMS, PET, and ITO was fixed to 100 μm, 130 μm, and 200 nm, respectively. The period and height of SWAs were set to be 155 and 180 nm, respectively, as observed by FE-SEM images (see Figure 3a). In Figure 2a, as the diameter to period ratio (R_{DP}) of SWAs on PDMS is increased to 0.65, the total transmittance over a wavelength range of 400−460 nm is also increased, and then it is gradually decreased at larger R_{DP} values than 0.65. It is also found that, at the R_{DP} value of 0.65 for SWAs with a 100 nm diameter, the total transmittance is >85% over the wavelength range of 400−460 nm. Moreover, at R_{DP} values of 0.6−0.7, the high average transmittance can be observed over a long wavelength region of 580−800 nm. From theoretical simulations, it is possible to achieve high transmittance in the PDMS layer when the diameter of SWAs is ∼100 nm. To achieve the transparent TENG device, a highly transparent SWA PDMS film and two transparent ITO-coated PET films as the top and bottom electrodes, respectively, were used to construct the entire device (Device-I). At the same time, we also fabricated another device (Device-II) by replacing the bare ITO/PET as a top electrode with the Au-coated ITO/PET. From the previous reports, it is very clear that polymer−electrode-based TENGs are more able to exchange triboelectric charges than polymer−polymer-based TENGs.[42] To design the polymer−electrode-based TENG device, the two different electrodes (ITO and Au) were employed and the output performance and transmittance of both devices were compared. The measured transmittance spectra of the TENG devices and

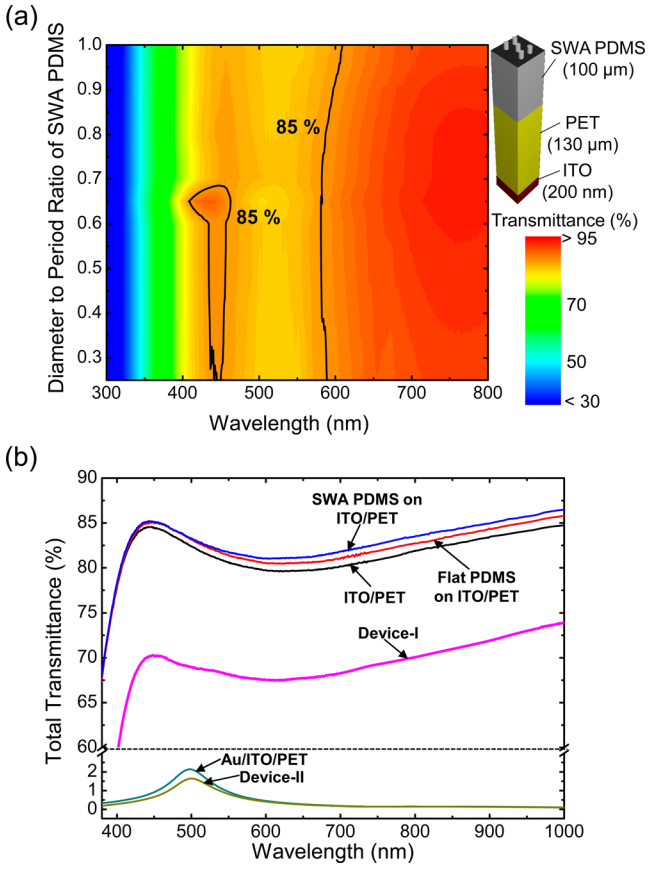

Figure 2. (a) Contour plot of variation of the calculated transmittance spectra of SWA PDMS on ITO/PET as functions of wavelength and diameter to period ratio (R_{DP}) of SWAs. (b) Measured transmittance spectra of the TENG devices and their constituent materials in the range of wavelengths from 380 to 1000 nm.

their constituent materials in the wavelength range of 380−1000 nm are shown in Figure 2b. The flat PDMS laminated on the PET surface of the ITO/PET substrate exhibited an improved average transmittance (T_{avg} ≈ 82%) compared to that of the bare ITO/PET substrate (T_{avg} ≈ 80.5%) in the visible and near-infrared wavelength regions. This increase in the transmittance spectra is due to the step gradient refractive index profile of air (n = 1)/PDMS (n ≈ 1.4)/PET (n ≈ 1.6). However, for the SWA PDMS laminated on the ITO/PET substrate, the average transmittance (T_{avg} ≈ 83%) was further enhanced and its total transmittance was higher than 85% over a wavelength range of 430−455 nm. From this, the SWAs can more effectively reduce the surface reflection because of a continuous linear gradient in the effective refractive index between air and the PDMS.[29,37] For the entire TENG device (Device-I), the high T_{avg} value of ∼70% was achieved at wavelengths of 400−1000 nm. Another TENG device (Device-II) exhibited a significantly lower average transmittance of ∼0.4% compared with that of the Device-I; this is attributed to the replacement of the Au-coated ITO/PET (T_{avg} ≈ 0.5%) with the bare ITO/PET (T_{avg} ≈ 81%) as a top electrode.

Figure 3a shows the top-view and cross-sectional SEM images of the nanoporous AAO template on a Si substrate. The SEM images of the SWA PDMS (using *h*-/*s*-PDMS) layer replicated by the AAO template are also shown. To examine the feasibility of nanostructures imprinted by the AAO template, the *h*-PDMS and *s*-PDMS layers were compared to

DOI: 10.1021/acsami.5b05842
ACS Appl. Mater. Interfaces 2015, 7, 20520−20529

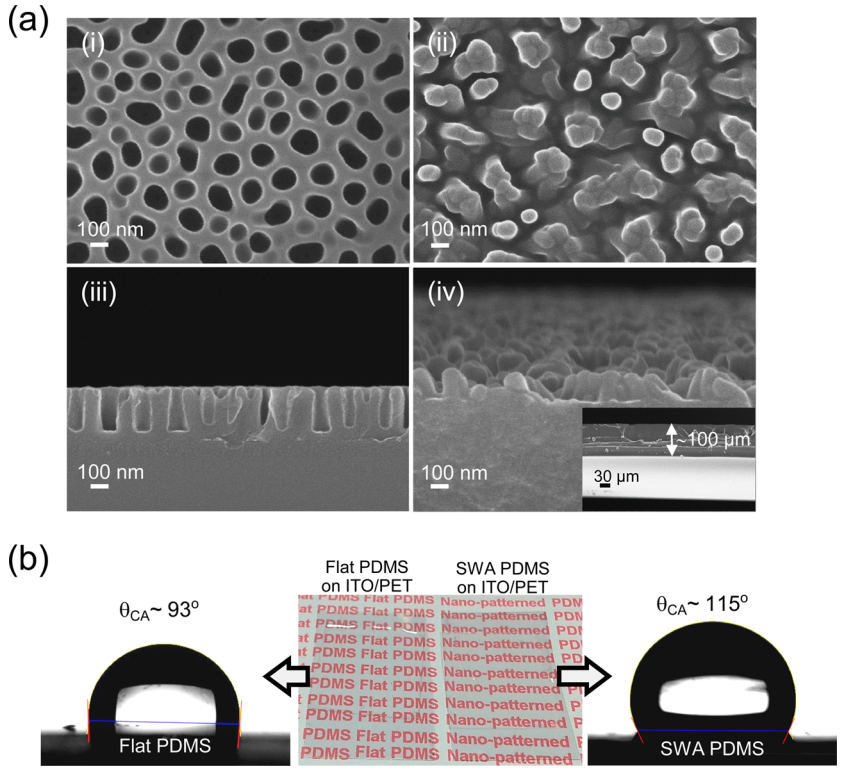

Figure 3. (a) Top-view and cross-sectional SEM images of the nanoporous AAO template on a Si substrate (i and iii) and the SWA PDMS (ii and iv) replicated by the AAO template. The inset of (iv) also shows the total thickness of the replicated PDMS layer. (b) Photographs of the flat and SWA PDMS layers on ITO/PET and the water droplets on the corresponding samples.

each other, as shown in Figure S1. The corresponding SEM images in Figure S1 reveal that only *s*-PDMS is not suitable for replicating the AAO nano features on the surface of the PDMS layer due to its lower modulus of ~2 N/mm^2 versus that (i.e., ~9 N/mm^2) of *h*-PDMS. The SEM images in i and iii of Figure 3a reveal that the average pore diameter, period, and height of AAO nanopores were approximately 100, 160, and 210 nm, respectively. The SEM images in ii and iv of Figure 3a show the uniformly distributed SWA arrays on the surface of PDMS, with an average diameter and height of ~100 and ~180 nm, respectively. The diameter and height of the SWAs were similar to the pore diameter and height of the nanoporous AAO template. Most of the SWAs were vertically oriented on the substrate, which produces shapes like a bunch because of the attractive forces among the SWAs of PDMS when they were pulled out from the AAO template. The total thickness of the replicated PDMS layer was observed to be ~100 μm, as can be seen in inset iv of Figure 3a. In Figure 3b, the photograph clarified that the SWA PDMS on ITO/PET is more transparent under the florescent light compared to the flat PDMS on ITO/PET. To explore the surface wettability of the flat and SWA PDMS, the water contact angle was estimated, and both samples (see Figure 3b) showed a hydrophobic surface with water contact angles (θ_{CA}) of >90°. However, the SWA PDMS exhibited a θ_{CA} value of ~115° that was larger than that (i.e., θ_{CA} ~ 93°) of the flat PDMS.[41,43] This SWA PDMS film with a hydrophobic surface (i.e., $\theta_{CA} \approx 115°$) can be utilized for self-cleaning applications.[41]

The working principle of the TENG device for generating the electrical energy is explained in Figure 4a. At the original position (i), two electrodes are separated with a constant distance (~3 mm) in the absence of an external pushing force. When an external pushing force is applied to the top electrode of the TENG device (ii), the ITO film of the ITO/PET substrate and the SWA PDMS film come into contact. As a result, because of the different triboelectric coefficients of SWA PDMS and ITO materials, the opposite electrostatic charges are induced on each electrode. The positive triboelectric charges accumulate on the ITO, and the negative charges are induced on the PDMS side.[30,44] When the applied pushing force is released from the device (iii), two electrodes move apart from each other and produce the induced potential difference across the electrodes. This potential difference drives the electrons from the bottom electrode to the top electrode and thus forms the negative current. When the device electrodes revert back to their original positions (iv), the triboelectric charge distribution reaches electrical equilibrium. Subsequently, as the external pushing force is applied once again (v), the electrons are driven toward the bottom electrode because of the reversed induced potential difference across the electrodes, which results in a positive current. To evaluate the performance of the TENG devices, a pressure indicator with a load cell (BONGSHIN, Inc.) was used to monitor (or adjust) the external pushing force to the device, with controlled frequencies using a metronome,[22,23] as shown in Figure S2. The V_{OC} curves generated by two different types of TENG devices (Device-I and Device-II) under 0.5 Hz of external pushing frequency and 0.3 kgf of external pushing force are shown in Figure 4b. The averaged V_{OC} values of Device-I and Device-II were observed as ~3.8 and ~2.2 V, respectively, in the shortest time interval (~0.25 s). These V_{OC} values are relatively low compared to those (i.e., V_{OC} > 10−200 V) reported for the PDMS-based TENG devices in previous works.[42,45,46] In general, however, the output voltage not only is directly proportional to the

DOI: 10.1021/acsami.5b05842
ACS Appl. Mater. Interfaces 2015, 7, 20520−20529

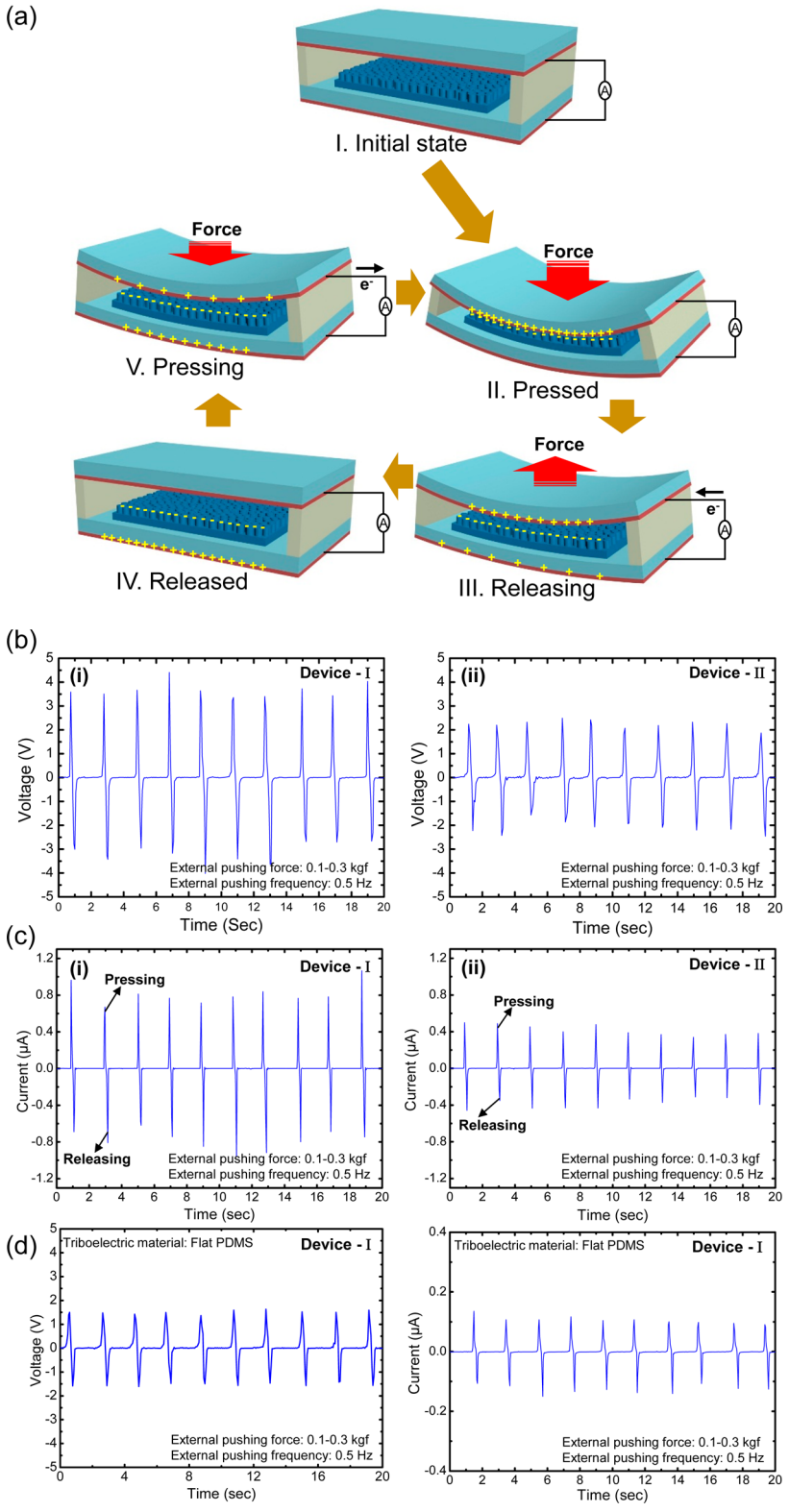

Figure 4. (a) Schematic illustration of the charge distribution process at each step of the TENG device and its working principle. Measured (b) V_{OC} and (c) I_{SC} curves of the TENG devices using (i) ITO/PET and (ii) Au-coated ITO/PET as top electrodes; during the measurements, the pushing frequency and pushing force are maintained at 0.5 Hz and 0.3 kgf, respectively. For comparison, the measured V_{OC} and I_{SC} curves of the TENG device fabricated by the flat PDMS on ITO/PET are compared in (d).

triboelectric surface charge density (σ) but also relates to the capacitance of the device.[47−50] Moreover, σ is mainly affected by the intrinsic material properties of the triboelectric (dielectric material) layer, the size of the dielectric, and the gap between the top electrode and dielectric as well as the roughness of the contact surfaces. Thus, it is necessary to improve the output voltage of TENG devices by further optimizing the area of SWA PDMS or the gap between SWA

DOI: 10.1021/acsami.5b05842
ACS Appl. Mater. Interfaces 2015, 7, 20520−20529

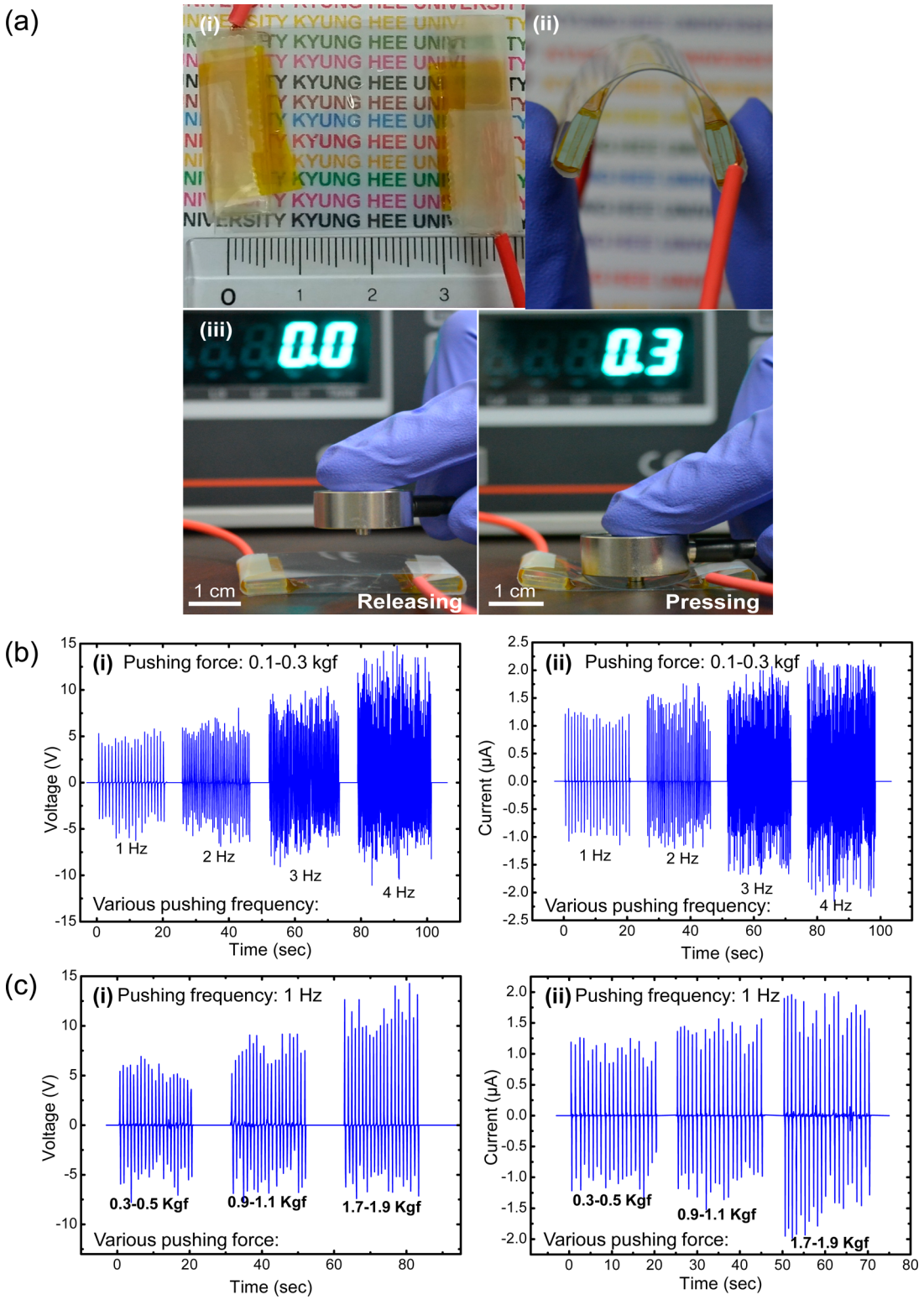

Figure 5. (a) Photographic images of the fabricated transparent TENG device for (i) high transparency, (ii) good flexibility, and (iii) the pushing test. (b and c) Measured (i) V_{OC} and (ii) I_{SC} curves (b) under different external pushing frequencies from 1 to 4 Hz at a 0.3 kgf external pushing force and (c) under 1 Hz of external pushing frequency at different external pushing forces.

PDMS and the top electrode. To optimize the distance between the SWA PDMS and the top electrode of the TENG device, we tested the influence of spacer thickness of the TENG device on the device output performance, as shown in Figure S3. From these results, we obtained the optimal spacer thickness of 3 mm for the TENG device, exhibiting stable and continuous output device performance. As a result, we used it in this experiment. Under the same condition, the I_{SC} curves of these devices were measured, as shown in Figure 4c. At the pressing and releasing moments on the device, the current peak directions were followed as indicated in Figure 4c, and they were well consistent with the charge flow of the schematic

DOI: 10.1021/acsami.5b05842
ACS Appl. Mater. Interfaces 2015, 7, 20520−20529

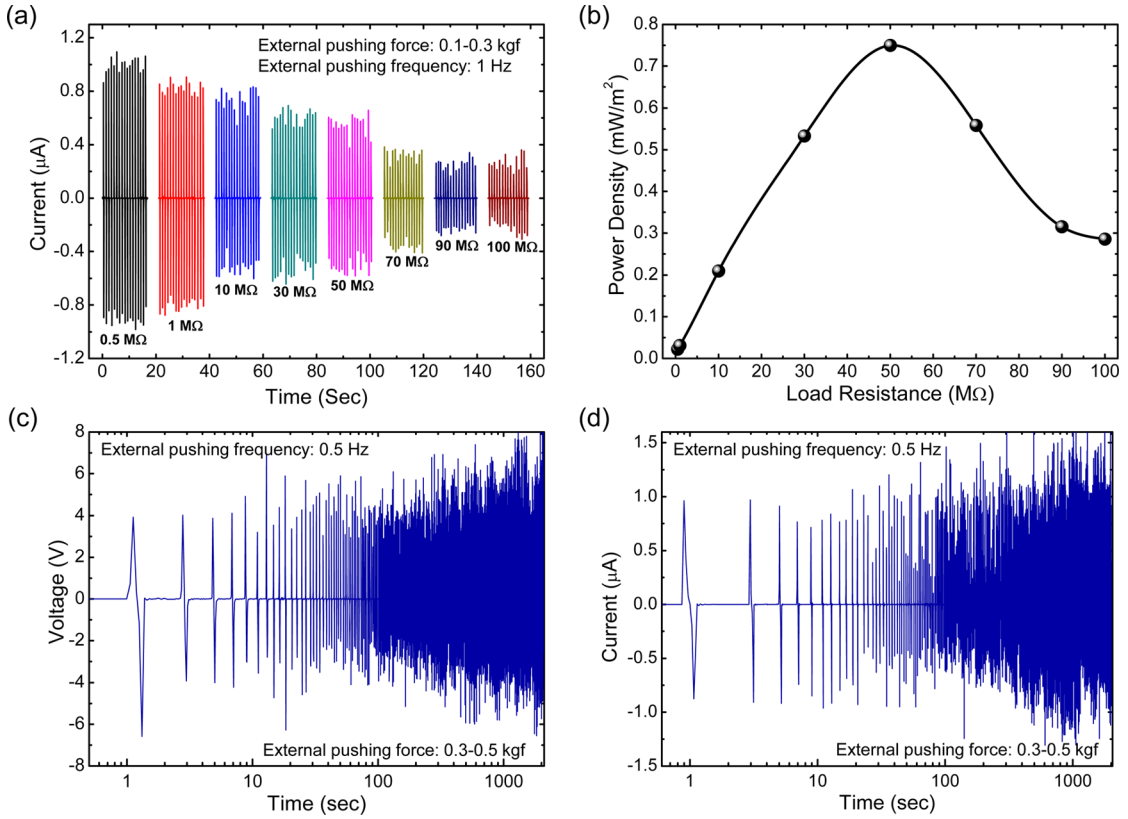

Figure 6. (a) Measured output current of the transparent TENG device at different load resistances under an external pushing force in the range of 0.1−0.3 kgf and at an external pushing frequency of 1 Hz. (b) Obtained average power density values of the transparent TENG device as a function of load resistance. (c and d) Robustness test of the transparent TENG: output (c) voltage and (d) current of the TENG device for 2000 s (i.e., 1000 cycles) under an external pushing force of 0.3−0.5 kgf and at a frequency of 0.5 Hz.

diagram in Figure 4a. Device-I and Device-II exhibited averaged I_{SC} values of ∼0.8 and ∼0.4 μA, respectively, in the short time interval (∼0.16 and 0.14 s, respectively). From these results, the output performance of Device-I is higher than that of Device-II. This may be the reason that the ITO (top electrode of Device-I) has a better friction surface to easily contact with the PDMS surface, and thus, it can sufficiently transfer more electrons into the device compared to the Au-coated ITO (top electrode of Device-II) surface, resulting in superior output device performance. It is also noticeable that the transmittance of Device-I is very high versus that of Device-II. Because of the high transmittance and output performance, Device-I with ITO/PET as a top electrode was further studied, while maintaining transparency. Moreover, to study the influence of the patterned PDMS surface (SWA PDMS) on device performance, we measured the TENG output performance using the flat PDMS as a triboelectric material instead of SWA PDMS as shown in Figure 4d. The results clearly show that the output performance of TENG using the flat PDMS (V_{OC} and I_{SC} values of ∼1.5 V and 0.13 μA, respectively) was relatively lower than that of TENG using the SWA PDMS. The increased surface area by SWA PDMS can be expected to offer enhanced triboelectric charges because of the large friction area, while the insufficient friction area between the flat PDMS and electrodes does not properly produce the triboelectric charges.[51,52]

Figure 5a shows the photographic images of the fabricated transparent TENG device by highlighting (i) transparency and (ii) flexibility. This image supports the high transmittance from measured transmittance data (see Figure 2b), and the device can be viewed by the colored background. The photographic images for the pushing test with a highly transparent and flexible TENG device are also shown in iii of Figure 5a. By using a load cell, a pushing force applied externally to the top electrode generates the electrostatic charges on the electrode surfaces according to the triboelectric tendency, as explained in Figure 4a. To examine the influence of external pushing frequency on the output performance of the transparent TENG device, the (i) V_{OC} and (ii) I_{SC} curves were measured at different external pushing frequencies from 1 to 4 Hz as shown in Figure 5b. During these measurements, the external pushing force was kept constant at 0.3 kgf. It is evident that V_{OC} and I_{SC} were gradually increased with an increase in the external pushing frequency. As the external pushing frequency increased from 1 to 4 Hz, the averaged voltage and current values were increased from ∼4.8 V and 1.2 μA to ∼11.6 V and 2.11 μA, respectively. As the external pushing frequency was increased, the output performance of the TENG was improved by the strongly accumulated residual charges on the surfaces of both electrodes due to the faster pushing cycle, thus leading to the increase in triboelectric potential.[51] Figure 5c shows the measured (i) V_{OC} and (ii) I_{SC} curves of the transparent TENG device under 1 Hz of external pushing frequency at different external pushing forces. As can be seen in the measured output curves, it can be known that the electric output of the TENG device is strongly related to the external pushing force, so the highest output can be observed under the largest external applied force. Over a small pushing force range of 0.3−0.5 kgf, the averaged V_{OC} and I_{SC} values of the TENG device were determined to be ∼5.1 V and ∼1.22 μA, respectively. When the external pushing force increased to

DOI: 10.1021/acsami.5b05842
ACS Appl. Mater. Interfaces 2015, 7, 20520−20529

1.7−1.9 kgf, the averaged V_{OC} and I_{SC} values increased to ∼10.2 V and ∼1.68 μA, respectively. This result is caused by the increased contact area and the deformation of PDMS under the strongest external pushing force.[23]

To investigate the effect of external load resistance on the output performance of the transparent TENG device, the output current and averaged power density were described. Figure 6a shows the measured output current of the transparent TENG device with different external load resistances in the range of 0.5−100 MΩ. These measurements of the transparent TENG device with different load resistances were performed under an external pushing force and a frequency of 0.1−0.3 kgf and 1 Hz, respectively. During the measurements, the contacting area between the top electrode and dielectric (SWA PDMS) material was observed as 1 cm^2, and the area of SWA PDMS of the TENG device during the measurement was also indicated in Figure S4. In Figure 6a, the output current was gradually decreased with an increase in load resistance due to ohmic losses. The average output current (I_{SC}) values were observed as ∼0.99, 0.82, 0.74, 0.61, 0.55, 0.33, 0.25, and 0.22 μA for load resistances of 0.5, 1, 10, 30, 50, 70, 90, and 100 MΩ, respectively. To calculate the averaged power density, we assumed that the electric energy was equivalent to the Joule heating energy. Thus, the averaged power density was obtained by[28,49]

$$\sum_{i=1}^{N} R \int_{t_{1i}}^{t_{2i}} \frac{I_i^2(t)}{N(t_{2i} - t_{1i})} \, dt$$

where N is the number of peaks, R is the external load resistance, and $I(t)$ is the output current as a function of time. The time between t_{1i} and t_{2i} is the interval time of the ith peak of the measured current. Figure 6b shows the variation of the obtained average power density per unit area of the transparent TENG device as a function of load resistance. It was found that the maximal average power density (W_{avg}) value of ∼0.75 mW/m^2 was achieved at a load resistance of 50 MΩ. Finally, the robustness of the transparent TENG device was tested by measuring the output voltage and current for 2000 s (i.e., 1000 cycles), as shown in Figure 6c and 6d. These voltage and current measurements were performed under an external pushing force of 0.3−0.5 kgf and at a frequency of 0.5 Hz. The transparent TENG device with SWA PDMS as a triboelectric material exhibited a consistently similar tendency in both the output voltage and current even after 1000 cycles without any significant degradation. Thus, these stable and continuous output voltage and current results up to 1000 cycles strongly support the possibility that the SWAs on PDMS could be maintained to produce triboelectric charges for many operating cycles.

CONCLUSIONS

In summary, we demonstrated the highly transperent and flexible TENG device with a SWA PDMS layer as the triboelectric material, fabricated by a simple and cost-effective process. The PDMS layer with SWAs was prepared by the replication from the nanoporous AAO template as a mold. The SWA PDMS on ITO/PET exhibited a relatively high tansmittance, which leads to a TENG device with a transmittance of ∼70% over a wavelength range of 400−1000 nm. The transparent TENG device with a bare ITO/PET top electrode exhibited higher output performance compared to that of the TENG device with Au-coated ITO/PET as the top electrode. Under an external pushing force of 0.3 kgf, the V_{OC} and I_{SC} values of the transparent TENG device (bare ITO/PET as the top electrode) were determined to be ∼3.8 V and ∼0.8 μA, respectively, at an external pushing frequency of 0.5 Hz. Furthermore, the output performance of the transparent TENG device was observed at different external pushing frequencies and pushing forces, indicating the improved device performance due to the large friction and contact area between the two electrodes. The maximal W_{avg} value of ∼0.75 mW/m^2 was achieved at a load resistance of 50 MΩ. These fabrication methods and results can be useful for achieving transparent, flexible, and cost-effective TENG devices with high output performance.

ASSOCIATED CONTENT

Supporting Information

The Supporting Information is available free of charge on the ACS Publications website at DOI: 10.1021/acsami.5b05842.

SEM image of the SWAs prepared by soft PDMS (Figure S1), PDMS spin-coating conditions, photographic images of pushing load cell, and indicator (Figure S2), TENG device performance with different spacer thicknesses (Figure S3), and areas of the SWA PDMS layer laminated on the ITO/PET of the TENG device (Figure S4) (PDF)

AUTHOR INFORMATION

Corresponding Author

*E-mail: jsyu@khu.ac.kr.

Notes

The authors declare no competing financial interest.

ACKNOWLEDGMENTS

This work was supported by a National Research Foundation of Korea (NRF) grant funded by the Korean government (MSIP) (2014-069441).

REFERENCES

(1) Wang, Z. L.; Wu, W. Nanotechnology-Enabled Energy Harvesting for Self-Powered Micro-/Nanosystems. *Angew. Chem., Int. Ed.* **2012**, *51*, 11700−11721.

(2) Robel, I.; Subramanian, V.; Kuno, M.; Kamat, P. V. Quantum Dot Solar Cells. Harvesting Light Energy with CdSe Nanocrystals Molecularly Linked to Mesoscopic TiO_2 Films. *J. Am. Chem. Soc.* **2006**, *128*, 2385−2393.

(3) Chang, C.; Tran, V. H.; Wang, J.; Fuh, Y. K.; Lin, L. Direct-Write Piezoelectric Polymeric Nanogenerator with High Energy Conversation Efficiency. *Nano Lett.* **2010**, *10*, 726−731.

(4) Chen, X.; Xu, S.; Yao, N.; Shi, Y. 1.6 V Nanogenerator for Mechanical Energy Harvesting Using PZT Nanofibers. *Nano Lett.* **2010**, *10*, 2133−2137.

(5) Ko, Y. H.; Lee, S. H.; Yu, J. S. Performance Enhanced Piezoelectric ZnO Nanogenerators with Highly Rough Au Electrode Surfaces on ZnO Submicrorod Arrays. *Appl. Phys. Lett.* **2013**, *103*, 022911.

(6) Zhang, C.; Tang, W.; Han, C.; Fan, F.; Wang, Z. L. Theoretical Comparison, Equivalent Transformation, and Conjunction Operations of Electromagnetic Induction Generator and Triboelectric Nanogenerator for Harvesting Mechanical Energy. *Adv. Mater.* **2014**, *26*, 3580−3591.

(7) Yang, Y.; Guo, W.; Pradel, K. C.; Zhu, G.; Zhou, Y.; Zhang, Y.; Hu, Y.; Lin, L.; Wang, Z. L. Pyroelectric Nanogenerators for Harvesting Thermoelectric Energy. *Nano Lett.* **2012**, *12*, 2833−2838.

DOI: 10.1021/acsami.5b05842
ACS Appl. Mater. Interfaces 2015, 7, 20520−20529

(8) Yang, W.; Chen, J.; Zhu, G.; Yang, J.; Bai, P.; Su, Y.; Jing, Q.; Cao, X.; Wang, Z. L. Harvesting Energy from the Natural Vibration of Human Walking. *ACS Nano* **2013**, *7*, 11317−11324.
(9) Zhu, G.; Bai, P.; Chen, J.; Wang, Z. L. Power-generating Shoe Insole Based on Triboelectric Nanogenerators for Self-Powered Consumer Electronics. *Nano Energy* **2013**, *2*, 688−692.
(10) Chen, J.; Yang, J.; Li, Z.; Fan, X.; Zi, Y.; Jing, Q.; Guo, H.; Wen, Z.; Pradel, K. C.; Niu, S.; Wang, Z. L. Networks of Triboelectric Nanogenerators for Harvesting Water Wave Energy: A Potential Approach toward Blue Energy. *ACS Nano* **2015**, *9*, 3324−3331.
(11) Chen, J.; Zhu, G.; Yang, W.; Jing, Q.; Bai, P.; Yang, Y.; Hou, T. C.; Wang, Z. L. Harmonic-Resonator-Based Triboelectric Nanogenerator as a Sustainable Power Source and a Self-Powered Active Vibration Sensor. *Adv. Mater.* **2013**, *25*, 6094−6099.
(12) Yang, W.; Chen, J.; Jing, Q.; Yang, J.; Wen, X.; Su, Y.; Zhu, G.; Bai, P.; Wang, Z. L. 3D Stack Integrated Triboelectric Nanogenerator for Harvesting Vibration Energy. *Adv. Funct. Mater.* **2014**, *24*, 4090−4096.
(13) Guo, H.; Chen, J.; Yeh, M. H.; Fan, X.; Wen, Z.; Li, Z.; Hu, C.; Wang, Z. L. An Ultrarobust High-Performance Triboelectric Nanogenerator Based on Charge Replenishment. *ACS Nano* **2015**, *9*, 5577−5584.
(14) Zhu, G.; Chen, J.; Zhang, T.; Jing, Q.; Wang, Z. L. Radial-Arrayed Rotary Electrification for High Performance Triboelectric Generator. *Nat. Commun.* **2014**, *5*, 3426.
(15) Wang, Z. L. Triboelectric Nanogenerators as New Energy Technology for Self-Powered Systems and as Active Mechanical and Chemical Sensors. *ACS Nano* **2013**, *7*, 9533−9557.
(16) Yang, W.; Chen, J.; Wen, X.; Jing, Q.; Yang, J.; Su, Y.; Zhu, G.; Wu, W.; Wang, Z. L. Triboelectrification Based Motion Sensor for Human-Machine Interfacing. *ACS Appl. Mater. Interfaces* **2014**, *6*, 7479−7484.
(17) Yang, J.; Chen, J.; Su, Y.; Jing, Q.; Li, Z.; Yi, F.; Wen, X.; Wang, Z.; Wang, Z. L. Eardrum-Inspired Active Sensors for Self-Powered Cardiovascular System Characterization and Throat-Attached Anti-Interference Voice Recognition. *Adv. Mater.* **2015**, *27*, 1316−1326.
(18) Chen, J.; Zhu, G.; Yang, J.; Jing, Q.; Bai, P.; Yang, W.; Qi, X.; Su, Y.; Wang, Z. L. Personalized Keystroke Dynamics for Self-Powered Human-Machine Interfacing. *ACS Nano* **2015**, *9*, 105−116.
(19) Bai, P.; Zhu, G.; Jing, Q.; Wu, Y.; Yang, J.; Chen, J.; Ma, J.; Zhang, G.; Wang, Z. L. Transparent and Flexible Barcode Based on Sliding Electrification for Self-Powered Identification Systems. *Nano Energy* **2015**, *12*, 278−286.
(20) Zhu, G.; Yang, W. Q.; Zhang, T.; Jing, Q.; Chen, J.; Zhou, Y. S.; Bai, P.; Wang, Z. L. Self-Powered, Ultrasensitive, Flexible Tactile Sensors Based on Contact Electrification. *Nano Lett.* **2014**, *14*, 3208−3213.
(21) Lin, L.; Hu, Y.; Xu, C.; Zhang, Y.; Zhang, R.; Wen, X.; Wang, Z. L. Transparent Flexible Nanogenerator as Self-Powered Sensor for Transportation Monitoring. *Nano Energy* **2013**, *2*, 75−81.
(22) Choi, M. Y.; Choi, D.; Jin, M. J.; Kim, I.; Kim, S. H.; Choi, J. Y.; Lee, S. Y.; Kim, J. M.; Kim, S. W. Mechanically Powered Transparent Flexible Charge-Generating Nanodevices with Piezoelectric ZnO Nanorods. *Adv. Mater.* **2009**, *21*, 2185−2189.
(23) Ko, Y. H.; Nagaraju, G.; Lee, S. H.; Yu, J. S. PDMS-Based Triboelectric and Transparent Nanogenerators with ZnO Nanorod Arrays. *ACS Appl. Mater. Interfaces* **2014**, *6*, 6631−6637.
(24) Wang, Z. L. Triboelectric Nanogenerators as New Energy Technology and Self-Powered Sensors−Principles, Problems and Perspectives. *Faraday Discuss.* **2014**, *176*, 447.
(25) Wang, Z. L.; Chen, J.; Lin, L. Progress in Triboelectric Nanogenerators as a New Energy Technology and Self-Powered Sensors. *Energy Environ. Sci.* **2015**, *8*, 2250−2282.
(26) Zhu, G.; Peng, B.; Chen, J.; Jing, Q.; Wang, Z. L. Triboelectric Nanogenerators as a New Energy Technology: From Fundamentals, Devices, to Applications. *Nano Energy* **2015**, *14*, 126−138.
(27) Ko, Y. H.; Lee, S. H.; Leem, J. W.; Yu, J. S. High Transparency and Triboelectric Charge Generation Properties of Nano-patterned PDMS. *RSC Adv.* **2014**, *4*, 10216−10220.
(28) Zhu, G.; Lin, Z. H.; Jing, Q.; Bai, P.; Pan, C.; Yang, Y.; Zhou, Y.; Wang, Z. L. Toward Large-Scale Energy Harvesting by a Nanoparticle-Enhanced Triboelectric Nanogenerator. *Nano Lett.* **2013**, *13*, 847−853.
(29) Fan, F. R.; Lin, L.; Zhu, G.; Wu, W.; Zhang, R.; Wang, Z. L. Transparent Triboelectric Nanogenerators and Self-Powered Pressure Sensors Based on Micropatterned Plastic Films. *Nano Lett.* **2012**, *12*, 3109−3114.
(30) Fan, F. R.; Tian, Z. Q.; Wang, Z. L. Flexible Triboelectric Generator. *Nano Energy* **2012**, *1*, 328−334.
(31) Boden, S. A.; Bagnall, D. M. Tunable Reflection Minima of Nanostructured Antireflective Surfaces. *Appl. Phys. Lett.* **2008**, *93*, 133108.
(32) Yu, Z.; Gao, H.; Wu, W.; Ge, H.; Chou, S. Y. Fabrication of Large Area Subwavelength Antireflection Structures on Si Using Trilayer Resist Nanoimprint Lithography and Liftoff. *J. Vac. Sci. Technol., B: Microelectron. Process. Phenom.* **2003**, *21*, 2874−2877.
(33) Song, Y. M.; Choi, H. J.; Yu, J. S.; Lee, Y. T. Design of Highly Transparent Glasses with Broadband Antireflective Subwavelength Structures. *Opt. Express* **2010**, *18*, 13063−13071.
(34) Leem, J. W.; Song, Y. M.; Yu, J. S. Six-fold Hexagonal Symmetric Nanostructures with Various Periodic Shapes on GaAs Substrates for Efficient Antireflection and Hydrophobic Properties. *Nanotechnology* **2011**, *22*, 485304.
(35) Lee, W.; Park, S. J. Porous Anodic Aluminum Oxide: Anodization and Templated Synthesis of Functional Nanostructures. *Chem. Rev.* **2014**, *114*, 7487−7556.
(36) Kokonou, M.; Nassiopoulou, A. G.; Giannakopoulos, K. P. Ultra-Thin Porous Anodic Alumina Films with Self-Ordered Cylindrical Vertical Pores on a p-Type Silicon Substrate. *Nanotechnology* **2005**, *16*, 103−106.
(37) Schmid, H.; Michel, B. Siloxane Polymers for High-Resolution, High-Accuracy Soft Lithography. *Macromolecules* **2000**, *33*, 3042−3049.
(38) Truong, T. T.; Lin, R.; Jeon, S.; Lee, H. H.; Maria, J.; Gaur, A.; Hua, F.; Meinel, I.; Rogers, J. A. Soft Lithography Using Acryloxy Perfluoropolyether Composite Stamps. *Langmuir* **2007**, *23*, 2898−2905.
(39) Odom, T. W.; Love, J. C.; Wolfe, D. B.; Paul, K. E.; Whitesides, G. M. Improved Pattern Transfer in Soft Lithography Using Composite Stamps. *Langmuir* **2002**, *18*, 5314−5320.
(40) Choi, K. M.; Rogers, J. A. A Photocurable Poly-(dimethylsiloxane) Chemistry Designed for Soft Lithographic Molding and Printing in the Nanometer Regime. *J. Am. Chem. Soc.* **2003**, *125*, 4060−4061.
(41) Leem, J. W.; Kim, S.; Lee, S. H.; Rogers, J. A.; Kim, E.; Yu, J. S. Efficiency Enhancement of Organic Solar Cells Using Hydrophobic Antireflective Inverted Moth-Eye Nanopatterned PDMS Films. *Adv. Energy Mater.* **2014**, *4*, 1301315.
(42) Fan, F. R.; Luo, J.; Tang, W.; Li, C.; Zhang, C.; Tian, Z.; Wang, Z. L. Highly Transparent and Flexible Triboelectric Nanogenerators: Performance Improvements and Fundamental Mechanisms. *J. Mater. Chem. A* **2014**, *2*, 13219−13225.
(43) Lim, J. H.; Ko, Y. H.; Leem, J. W.; Yu, J. S. Improvement in Light Harvesting of Dye-Sensitized Solar Cells with Antireflective and Hydrophobic Textile PDMS Coating by Facile Soft Imprint Lithography. *Opt. Express* **2015**, *23*, A169−A179.
(44) Cross, J. A. *Electrostatics: Principles, Problems and Applications*; Adam Hilger: Bristol, U.K., 1987.
(45) Zhang, X. S.; Han, M. D.; Wang, R. X.; Meng, B.; Zhu, F. Y.; Sun, X. M.; Hu, W.; Wang, W.; Li, Z. H.; Zhang, H. X. High-Performance Triboelectric Nanogenerator with Enhanced Energy Density Based on Single-Step Fluorocarbon Plasma Treatment. *Nano Energy* **2014**, *4*, 123−131.
(46) Wang, S.; Lin, L.; Wang, Z. L. Nanoscale Triboelectric-Effect-Enabled Energy Conversion for Sustainably Powering Portable Electronics. *Nano Lett.* **2012**, *12*, 6339−6346.

DOI: 10.1021/acsami.5b05842
ACS Appl. Mater. Interfaces 2015, 7, 20520−20529

(47) Han, M.; Zhang, X. S.; Meng, B.; Liu, W.; Tang, W.; Sun, X.; Wang, W.; Zhang, H. r−Shaped Hybrid Nanogenerator with Enhanced Piezoelectricity. *ACS Nano* **2013**, *7*, 8554−8560.
(48) Tian, H.; Ma, S.; Zhao, H. M.; Wu, C.; Ge, J.; Xie, D.; Yang, Y.; Ren, T. L. Flexible Electrostatic Nanogenerator Using Graphene Oxide Film. *Nanoscale* **2013**, *5*, 8951−8957.
(49) Niu, S.; Wang, S.; Lin, L.; Liu, Y.; Zhou, Y. S.; Hu, Y.; Wang, Z. L. Theoretical Study of Contact-Mode Triboelectric Nanogenerators as an Effective Power Source. *Energy Environ. Sci.* **2013**, *6*, 3576−3583.
(50) Tang, W.; Zhou, T.; Zhang, C.; Fan, F. R.; Han, C. B.; Wang, Z. L. A Power-Transformed-and-Managed Triboelectric Nanogenerator and Its Applications in a Self-Powered Wireless Sensing Node. *Nanotechnology* **2014**, *25*, 225402.
(51) Zhang, X. S.; Han, M. D.; Wang, R. X.; Zhu, F. Y.; Li, Z. H.; Wang, W.; Zhang, H. X. Frequency-Multiplication High-Output Triboelectric Nanogenerator for Sustainably Powering Biomedical Microsystems. *Nano Lett.* **2013**, *13*, 1168−1172.
(52) Zhu, G.; Pan, C.; Guo, W.; Chen, C. Y.; Zhou, Y.; Yu, R.; Wang, Z. L. Triboelectric-Generator-Driven Pulse Electrodeposition for Micropatterning. *Nano Lett.* **2012**, *12*, 4960−4965.

DOI: 10.1021/acsami.5b05842
ACS Appl. Mater. Interfaces 2015, 7, 20520−20529